Journal of Power Sources 210 (2012) 327–338

Contents lists available at SciVerse ScienceDirect

Journal of Power Sources

journal homepage: www.elsevier.com/locate/jpowsour

Computational and experimental studies of laser cutting of the current collectors for lithium-ion batteries

Dongkyoung Lee[a], Rahul Patwa[c], Hans Herfurth[c], Jyotirmoy Mazumder[a,b,*]

[a] Center for Lasers and Plasmas for Advanced Manufacturing (CLPAM), Department of Mechanical Engineering, University of Michigan, Ann Arbor, MI 48109, United States
[b] Department of Material Science and Engineering, University of Michigan, Ann Arbor, MI 48109, United States
[c] Fraunhofer Center for Laser Technology, 46025 Port Street, Plymouth, MI 48170, United States

ARTICLE INFO

Article history:
Received 14 December 2011
Received in revised form 8 March 2012
Accepted 12 March 2012
Available online 20 March 2012

Keywords:
Laser cutting
Lithium-ion battery
Current collector
Computational model
Single mode fiber laser

ABSTRACT

Sizing electrodes is an important step during Lithium-ion battery manufacturing processes since poor cut edge affects battery performance significantly and sometime leads to fire hazard. Mechanical cutting could result in a poor cut quality with defects. The cutting quality can be improved by using a laser, due to its high energy concentration, fast processing time, small heat-affected zone, and high precision. The cutting quality is highly influenced by operating parameters such as laser power and scanning speed. Thus, we studied a numerical simulation to provide a guideline for achieving clear edge quality. In order to simulate electrodes laser cutting for Lithium-Ion batteries, understanding the behavior of current collectors is crucial. This study focuses on current collectors, such as pure copper and aluminium. Numerical studies utilized a 3D self-consistent mathematical model for laser–material interaction. Observations of penetration time, depth, and threshold during laser cutting processes of current collectors are described. The model is validated experimentally by cutting current collectors and single side-coated electrodes with a single mode fiber laser. The copper laser cutting is laser intensity and interaction time dependent process. The aluminium laser cutting depends more on laser intensity than the interaction time. Numerical and experimental results show good agreement.

1. Introduction

The automotive industry is strongly motivated to satisfy consumer demand for high fuel efficiency and environmental protection agency (EPA) emission regulation. To satisfy these requirements, there are efforts to accelerate the electrification of future powertrains. The market for hybrid electric vehicles (HEVs), plug-in hybrid electric vehicles (PHEVs) and electric vehicles (EVs) is rapidly expanding, especially, in the US and Japan [1]. To develop more efficient hybrid and electric vehicles, an understanding of automotive battery technology is essential. Among the many battery technologies, the lithium-ion battery represents the most promising technology for the abovementioned vehicles, because of their high energy-to-weight ratio, high power density, a lack of memory effect, and lighter weight than other energy-equivalent secondary batteries [2,3]. The lithium-ion battery consists of an anode, cathode, and electrolyte. The anode is usually graphite-coated copper and the cathode is lithium metal oxide-coated aluminum.

One of the important factors to affect the performance of the lithium-ion battery is the manufacturing process. Electrodes are produced as follows. A polymeric binder and solvent are mixed with active electrode powder material to slurry. A thin film of the slurry is spread onto both sides of a metal foil. Subsequently, the coated metal foil is cured in a drying oven. Then, the coated materials are cut to different sizes using mechanical tools. Currently, die cutting and rotary knife slitting are applied to size the electrodes used for prismatic and cylindrical cells, respectively. Both techniques require precise and relatively expensive tooling that wears over time. This tool wear results in process instability and poor cut quality. This poor cut quality, characterized by edge bending, burrs and delamination is a main cause of short circuits [1] and high heat generation inside the battery cell, which may result in the catastrophic failure of the entire module. Laser processing is proven in the industry as a highly efficient and reliable manufacturing method that can solve these problems since it has many

Abbreviations: L/V, liquid–vapor interface; S/L, solid–liquid interface; HEV, hybrid electric vehicle; PHEV, plug-in hybrid electric vehicle; EV, electric vehicle.

* Corresponding author at: Department of Mechanical Engineering, University of Michigan, Ann Arbor, MI 48109, United States. Tel.: +1734 647 6824; fax: +1 734 763 5772.
E-mail address: mazumder@umich.edu (J. Mazumder).

0378-7753/$ – see front matter © 2012 Elsevier B.V. All rights reserved.
doi:10.1016/j.jpowsour.2012.03.030

Nomenclature

Physical constant

R	gas constant, 8.314×10^{15} J K^{-1} mol^{-1}
σ	Stefan–Boltzmann constant, 5.67×10^{-8} W m^{-2} K^{-4}

Symbols

α	incident angle,°
A_0	absorption coefficient
C_{pl}	liquid constant-pressure specific heat, J kg^{-1} K^{-1}
C_{ps}	solid constant-pressure specific heat, J kg^{-1} K^{-1}
$\bar{C}_p$	average constant-pressure mixture specific heat, J kg^{-1} K^{-1}
$\bar{C}_{pl}$	average constant-pressure specific heat of liquid, J kg^{-1} K^{-1}
$\bar{C}_{ps}$	average constant-pressure specific heat of solid, J kg^{-1} K^{-1}
δ	delta function
$\mathbf{e}_x$, $\mathbf{e}_y$, $\mathbf{e}_z$	unit vectors in x, y, z directions, respectively
ε	emissivity
f_l	liquid mass fraction
f_s	solid mass fraction
g_l	liquid volume fraction
g_s	solid volume fraction
F	force function, m s^{-1}
F_{evap}	speed function of the L/V interface due to evaporation, m s^{-1}
h	enthalpy, J kg^{-1}
h_l	liquid enthalpy, J kg^{-1}
h_s	solid enthalpy, J kg^{-1}
$H_{\varepsilon,c}(\phi)$	smoothing function
i	incoming ray
k	thermal conductivity, W m^{-1} K^{-1}
k_l	liquid thermal conductivity, W m^{-1} K^{-1}
k_s	solid thermal conductivity, W m^{-1} K^{-1}
κ	curvature
L_m	latent heat of fusion, J kg^{-1}
L_v	latent heat of vaporization, J kg^{-1}
μ	viscosity, m^2 s^{-1}
μ_{vap}	vapor viscosity, m^2 s^{-1}
μ_{liq}	liquid viscosity, m^2 s^{-1}
$\dot{m}''_{evap}$	net mass loss due to evaporation per area, kg s^{-1} m^{-2}
$\mathbf{n}$	normal vector
p	pressure, Pa
ρ	density, kg m^{-3}
ρ_l	liquid density, kg m^{-3}
ρ_s	solid density, kg m^{-3}
$\dot{q}''$	the actual net energy influx at the liquid–vapor interface per area, J s^{-1} m^{-2}
$\dot{q}''_{L/V}$	the spatial laser beam distribution after multiple reflections per area, J s^{-1} m^{-2}
$\dot{q}''_{evap}$	energy loss due to evaporation per area, J s^{-1} m^{-2}
R_v	specific gas constant, J kg^{-1} K^{-1}
r	reflected ray
σ	surface tension, N m^{-1}
t	time, s
T	temperature, K
T_s	temperature at surface, K
T_m	melting temperature, K
T_b	boiling temperature, K
T_v	temperature at vapor, K
$\mathbf{u}$	fluid velocity vector, m s^{-1}
u_v	velocity of vapor, m s^{-1}
$\mathbf{x}$	spatial vector
ϕ	level set function

advantages, such as contact-free process, high energy concentration, fast processing speed, small heat-affected zone (HAZ) and flexibility of laser power.

The contact-free cutting of electrode with a single mode fiber laser for the lithium-ion battery has been investigated to determine the achievable cut quality [4,5]. A comparison between a CW mode and pulsed mode laser was studied to upscale the cutting speed while preserving the high cutting quality [6]. It is important to understand the physics associated with laser cutting to improve the performance of the battery. To the best of the authors' knowledge, it has not been studied so far. To fully understand the behavior of electrodes during the laser cutting, investigation of the behavior of the current collector materials is an essential step. Therefore, we focus on the current collector materials, such as aluminum and copper in this study.

Laser cutting involves phase changes, such as solidification, melting, and evaporation. A Knudsen layer on the liquid–vapor (L/V) interface, where the continuum hypothesis fails, is formed due to a high evaporation speed. Moreover, a deep penetration hole is observed prior to accomplishing the cutting as shown in Fig. 1, which requires the full penetration of the materials. When a deep penetration hole exists, laser energy can accumulate inside the hole so that the absorbed energy increases dramatically. This increased energy absorption might in turn expedite the penetration hole depth. Due to these physical characteristics, laser cutting promises cleaner and sharper edge compared to mechanical cutting.

Ki et al. developed a mathematical three-dimensional self-consistent laser–material interaction model with the aid of the level-set method [7–12]. This model includes fluid flow, heat transfer, phase changes, multiple internal reflections, free surface evolution, discontinuity at the L/V interface and surface forces on the steel. This model is utilized here with modifications in order to investigate the physical characteristics during laser cutting on the current collectors of the lithium-ion batteries.

First, this paper describes the mathematical model for three-dimensional self-consistent laser–material interaction applied to pure copper and aluminum foils. Second, the simulation results are analyzed and discussed taking into consideration the penetration

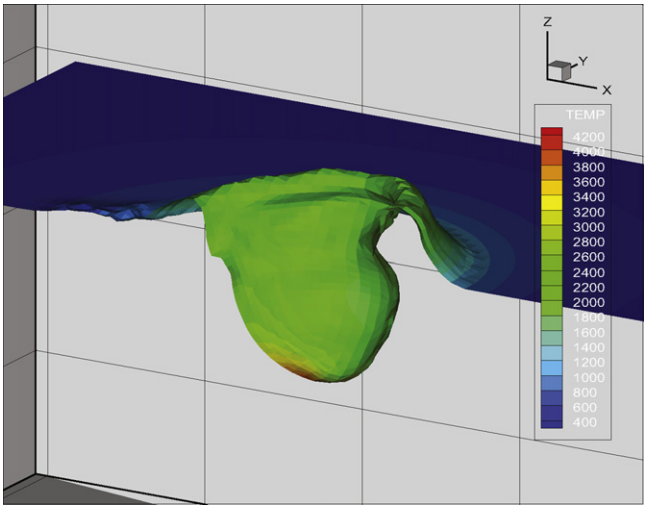

Fig. 1. A deep penetration hole during laser cutting of copper.

time and depth. Based on the numerical analysis, laser parameter thresholds are provided for the laser cutting of the current collector materials. Third, the simulation results are experimentally validated. Finally, the conclusion is presented.

2. Mathematical modeling

2.1. Governing equations

The three-dimensional self-consistent laser–material interaction model is summarized, closely following Ki et al. [12] with some modifications since pure aluminum and copper foils are selected as substrates. This study assumes an incompressible, laminar and Newtonian liquid flow. Vaporization processes are treated as the volume source. Continuity, momentum transfer, energy transfer can be expressed by following governing equations with boundary conditions.

$$\nabla \cdot \mathbf{u} = \frac{\dot{m}''_{evap}}{\rho}\delta(\phi) \tag{1}$$

$$\frac{\partial(\rho u)}{\partial t} + \nabla\cdot(\rho \mathbf{u} u) = \mu\nabla^2 u - \frac{\partial p}{\partial x} - \mathbf{e_x}\cdot\left(\sigma n\kappa - \nabla_s T\frac{d\sigma}{dT}\right)\delta(\phi) \tag{2}$$

$$\frac{\partial(\rho v)}{\partial t} + \nabla\cdot(\rho \mathbf{u} v) = \mu\nabla^2 v - \frac{\partial p}{\partial y} - \mathbf{e_y}\cdot\left(\sigma n\kappa - \nabla_s T\frac{d\sigma}{dT}\right)\delta(\phi) \tag{3}$$

$$\frac{\partial(\rho w)}{\partial t} + \nabla\cdot(\rho \mathbf{u} w) = \mu\nabla^2 w - \frac{\partial p}{\partial z} - \mathbf{e_z}\cdot\left(\sigma n\kappa - \nabla_s T\frac{d\sigma}{dT}\right)\delta(\phi) \tag{4}$$

$$\frac{\partial(\rho\bar{C}_{pl}T)}{\partial t} + \mathbf{u}\cdot\nabla(\rho\bar{C}_{pl}T) = \nabla\cdot(k\nabla T) - L\frac{\partial(\rho f_l)}{\partial t} + \frac{\partial(\rho f_s\Delta\bar{C}_p T)}{\partial t} + \dot{q}''(t,\mathbf{x})\delta(\phi) \tag{5}$$

where $\mathbf{u}$ is the liquid velocity vector, $\mathbf{x}$ is the spatial vector, ρ is the density, μ is the viscosity, p is the pressure, k is the thermal conductivity, $\bar{C}_{pl}$ is the average-specific heat of liquid, t is the time, f_l is the liquid mass fraction and $\delta(\phi)$ is the delta function to incorporate L/V boundary conditions. Third terms on the right hand side of Eqs. (2)–(4) are boundary conditions for the L/V interface. This model contains the capillary and thermo-capillary forces similar to Ki et al. [12]. The second and third terms on the right hand side of Eq. (5), which are the boundary conditions for energy equations on the S/L interface, are adopted from Bennon's continuum model [13]. The solid mass fraction is defined as

$$f_s = 1 - f_l \tag{6}$$

Similarly, the volume fraction can be defined for liquid and solid (g_l and g_s). The relationship between the mass fraction (f_l) and the volume fraction (f_s) can be described as

$$f_s = \frac{\rho_s g_s}{\rho} \tag{7}$$

$$f_l = \frac{\rho_l g_l}{\rho} \tag{8}$$

$$g_s + g_l = 1 \tag{9}$$

With these relations, the density (ρ), thermal conductivity (k), and enthalpy (h) for the liquid and solid mixture are defined as

$$\rho = g_s\rho_s + g_l\rho_l \tag{10}$$

$$k = \left(\frac{g_s}{k_s} + \frac{g_l}{k_l}\right)^{-1} \tag{11}$$

$$h = f_s h_s + f_l h_l \tag{12}$$

This model assigns the mass liquid fraction 1 and 0 when the temperature is above and below melting temperature, respectively, since pure materials have been selected. The phase enthalpies are obtained as

$$h_s = \int_0^T C_{ps}\ dT \tag{13}$$

$$h_l = \int_0^{T_m} C_{ps}\,dT + L_m + \int_{T_m}^T C_{pl}\,dT \tag{14}$$

where T_m is the melting temperature, L_m is the latent heat of fusion, C_{pl} is the constant-pressure specific heat of liquid, C_{ps} is the constant-pressure specific heat of the solid. Furthermore, the average specific heats of solid and liquid ($\bar{C}_{ps}$ and $\bar{C}_{pl}$) are defined as

$$\bar{C}_{ps} = \frac{1}{T}\int_0^T C_{ps}\ dT \tag{15}$$

$$\bar{C}_{pl} = \frac{1}{T - T_m}\int_{T_m}^T C_{pl}\ dT \tag{16}$$

$$h_s = \bar{C}_{ps}T \tag{17}$$

$$h_l = \bar{C}_{ps}T_m + L_m + \bar{C}_{pl}(T - T_m) = \bar{C}_{pl}T + L \tag{18}$$

$$\bar{C}_p = \bar{C}_{pl} - f_s(\bar{C}_{pl} - \bar{C}_{ps}) \tag{19}$$

where $L = (\bar{C}_{ps} - \bar{C}_{pl})T_m + L_m$. By using the defined mixture variables, the boundary conditions for S/L interface can be calculated [9]. The energy source term, which is a fourth term on the right hand side of Eq. (5), is added into the energy conservation equation as the boundary condition of the L/V interface in Eq. (5). A detailed explanation of this term will be discussed later in the multiple reflections section.

2.2. Level set equation for the L/V interface tracking

The tracking free surface plays an important role in the investigation of the interface shape and the process physics. The level set method was developed by Osher and Sethian [14]. This method has increasingly been used for many complex problems because of following reasons. First, it is easy to implement and conceptually straightforward. Second, surface merging and separation can be automatically handled. Third, geometric qualities, such as the surface normal and the curvature on the surface, are easy to calculate.

To implement the level set method, the surface of interest, which is the L/V interface, is set as the zero iso-surface or zero level set. However, the equations are valid for both a zero level set, as well as all other level sets [15].

$$\phi(\mathbf{x}, t) = \pm d \tag{20}$$

To derive PDE, d in Eq. (20) is set to zero and the material derivative is taken as

$$\frac{D\phi}{Dt} = \frac{\partial\phi}{\partial t} + u\cdot\nabla\phi = 0 \tag{21}$$

This equation can be re-written as

$$\frac{\partial\phi}{\partial t} + u\cdot\mathbf{n}|\nabla\phi| = 0 \tag{22}$$

Since surface normal vectors can be obtained from the level set function as

$$\mathbf{n} = \frac{\nabla\phi}{|\nabla\phi|} \tag{23}$$

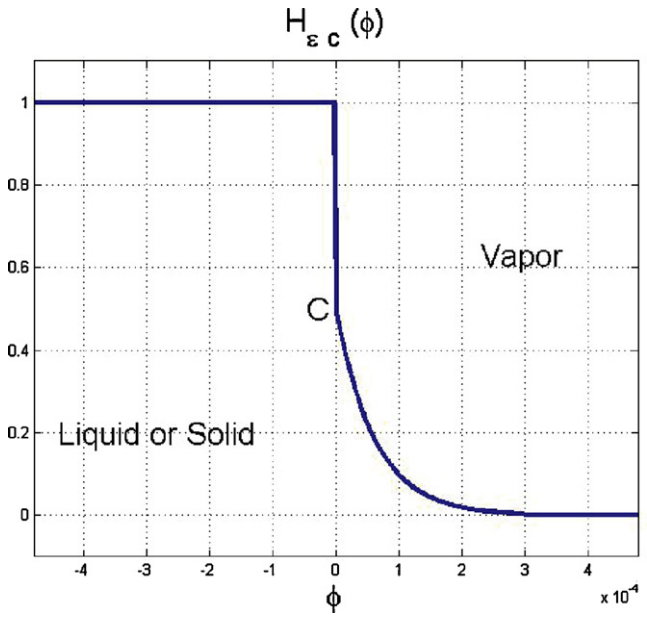

Fig. 2. Smoothing material properties.

Here, $\mathbf{u}\cdot\boldsymbol{n}$ is the speed of the interface in the normal direction and F is referred to as the speed function or force function. Thus, the final form of the level set function is a hyperbolic PDE.

$$\frac{\partial\phi}{\partial t} + F|\nabla\phi| = 0 \tag{24}$$

The speed function in this study is discussed later in detail.

2.3. Smoothing material properties near the L/V

The L/V interface has significantly different properties to those of the S/L interface. Therefore, the material properties are smoothed out from the liquid to the vapor phase using discrete functions proposed as

$$H_{\varepsilon,c}(\phi) = \begin{cases} 1 & \text{if } \phi \le 0, \\ c\left(\frac{1}{2}\right)^{\phi/\min(\Delta z)} & \text{if } 0 < \phi \le \varepsilon, \\ 0 & \text{iif } \phi > \varepsilon, \end{cases} \tag{25}$$

where ε and c represent the width of the interface and the degree of continuity, respectively. The c ranges from 0 to 1. Thus, the material properties can be expressed by this function. This is shown in Fig. 2. Viscosity, for example, is defined as

$$\mu_{\varepsilon,c} = \mu_{vap} + (\mu_{liq} - \mu_{vap})H_{\varepsilon,c}(\phi) \tag{26}$$

2.4. Modeling of L/V interface phenomena

In the laser–material interaction processes, the L/V interface in the level set equation, i.e. $\phi = 0$, is evolved on the basis of fluid flow and vaporization. The fluid flow can be obtained by solving momentum equation proposed in Eq. (3). To implement vaporization into the level set equation, jump conditions with back pressure is used to take into account discontinuity at the interface cause by the Knudsen layer [16]. The net mass flux and energy flux [7,16,17] can be obtained as

$$\dot{m}''_{evap} = \rho_s\sqrt{\frac{RT_s}{2\pi}} - \rho_v\sqrt{\frac{RT_v}{2\pi}}\beta F_-(m) = \rho_l F_{evap} \tag{27}$$

$$\dot{q}''_{evap} = \rho_l L_v F_{evap} \tag{28}$$

where

$$m = \frac{u_v}{\sqrt{2R_vT_v}}$$

$$F_- = \sqrt{\pi}m[-1 + erf(m)] + \exp(-m^2)$$

$$G_- = (2m^2+1)[1 - erf(m)] - \frac{2}{\sqrt{\pi}}m\exp(-m^2)$$

$$\beta = \frac{2(2m^2+1)\sqrt{T_v/T_s} - 2\sqrt{\pi}m}{F_- + \sqrt{T_v/T_s}G_-}$$

Hence, a final form of the speed function is

$$F = F_{evap} + \mathbf{u}\cdot\mathbf{n} \tag{29}$$

where $\mathbf{u}$ is the melt pool speed and $\mathbf{n}$ is the normal vector. The vaporizing mass flux, F_{evap}, can be assumed perpendicular to the L/V interface.

2.5. Multiple reflections with incident angle

The energy absorption during the laser cutting process is greater than the energy absorption on a flat material surface. The portion of total energy transferred from the laser beam to a workpiece can be increased dramatically when the deep penetration hole exists due to the multiple reflections inside the walls of the hole. These multiple reflections can be identified by using the ray tracing method. If the laser beam is irradiated on the wall of the deep penetration hole, then the reflected rays can be calculated by

$$r = i + 2(-i\cdot\mathbf{n})\mathbf{n} \tag{30}$$

where r is the reflected ray, i is the incoming ray, and n is the surface unit normal. A surface unit normal vector can be obtained at each point with the aid of the level-set method. In this method, the laser energy is absorbed into the wall at each reflection. When the rays escape the computational domain, the calculation of the multiple reflections is terminated. Furthermore, incident angle is taken into account in determining the absorption coefficient, suggested by Fabbro and Chouf [18]. It is presented as following

$$A(\alpha) = A_0(\cos\,\alpha)^q \tag{31}$$

where α is the incident angle, α is the absorption coefficient on flat surface, and A_0 is the characteristic of the material. Again, the incident angle can be calculated based on the information from the level-set method. The values of the material characteristics, such as for A_0 and q, vary based on the material properties. The multiple reflections contribute a large portion of the laser energy absorption in the deep penetration hole during laser material interaction and it increases absorption dramatically compared to the absorption on the flat surface. This increased energy absorption by multiple reflections causes the metal to behave as a black body. After considering energy losses due to evaporation and radiation, the actual net energy influx at the interface is

$$\dot{q}'' = \dot{q}''_{L/V} - \dot{q}''_{evap} - \sigma\varepsilon(T^4 - T_\infty^4) \tag{32}$$

where $\dot{q}''_{L/V}$ is the spatial laser beam distribution after multiple reflections $\sigma\varepsilon(T^4 - T_\infty^4)$ is energy loss due to radiation, σ and ε are Stefan–Boltzmann constant and emissivity, respectively. Note that the simultaneous calculation of the vapor phase and the liquid phase allows for the exclusion of convection heat loss [12].

3. Experiments

The schematic of the remote laser cutting process is shown in Fig. 3. An IPG single mode cw IR fiber laser working at 1070 nm with maximum output power of 500 W is used as the laser source. The laser beam is fiber-delivered using a 10 μm core-fiber diameter

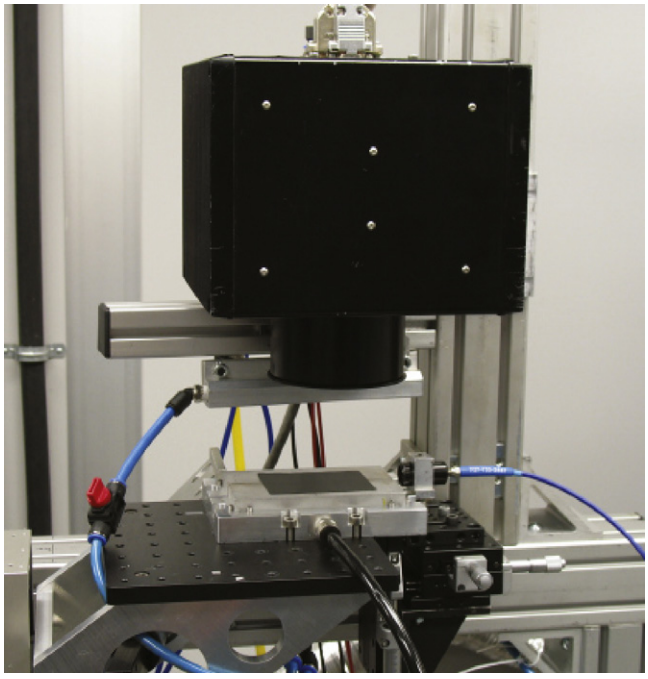

Fig. 3. Experimental setup.

and is collimated to a beam diameter of 13 mm. A 2D galvo-scanner from Scanlab is used to deflect and move the laser beam at high dynamic speeds with maximum speeds up to 5 m s^{-1}. A 80 mm F-theta objective mounted on the scanner keeps the scanning image field flat within a 35 mm × 35 mm square field size. The measured spot size at the focus position is approximately 11 μm with a small Rayleigh length of 70 μm and M2 value (86%) of 1.3. The spot is symmetrical and has a closely Gaussian energy distribution. Given the small Rayleigh length, it is essential to hold the material flat on the fixture during the entire cutting process. A vacuum fixture is used to hold electrodes and prevent any movement during the cutting process. A narrow groove (<1 mm) is machined in the top plate of the fixture right underneath where the cutting takes place to prevent any melt attachments that come out of the cutting kerf. The fixture is mounted horizontally on two orthogonal axes of a CNC motion system while the scanner is mounted on its third vertical axis. This precise 3-axis positioning is required for the setup to align the fixture with the scanner and to position the scanner at the correct vertical distance from the electrode foil. There is no process gas applied during cutting. Cutting is performed in a clean and dust free environment with suitable fume exhaust systems.

Materials used for laser cutting pure copper and aluminum foils with a thickness of 10 μm and 15 μm, respectively. In addition, single side-coated electrodes with the thickness of 100 μm are considered to validate the mathematical model in a more realistic situation. The thickness of graphite on the top of copper is 90 μm. $LiCoO_2$ with the thickness of 85 μm is coated on the top of aluminum. The electrodes placed on the fixture as the active electrode materials face upward and the laser beam irradiates on the surface of active electrode materials.

4. Results and discussion

4.1. Simulation preparations and solution schemes

The numerical domain of simulation is 75 μm × 30 μm × 75 μm with the non-uniform mesh size. A staggered grid is used to obtain the physically proper pressure field [19]. The smallest discrete mesh distance is 0.42857 μm. Pure copper and aluminum are chosen as the substrate materials. The properties of these materials are shown in Tables 1 and 2.

Table 1
Material properties of copper.

Property	Value
Melting temperature	1357.77 (K)
Normal boiling temperature	2835.15 (K)
Critical point temperature	8280 (K)
Liquid density	7920 (kg m^{-3})
Solid density	8960 (kg m^{-3})
Kinematic viscosity	3.50E−07 (m^2 s^{-1}) [21]
Surface tension	$1.257 - 0.0002 \times (T - 1356)$ (N m^{-1}) [22]
Latent heat of vaporization	5.23E+06 (J kg^{-1})
Latent heat of fusion	2.05E+05 (J kg^{-1})
Solid thermal conductivity	317 (W m^{-1} K^{-1}) [23]
Liquid thermal conductivity	157 (W m^{-1} K^{-1}) [23]
Liquid constant-pressure specific heat	571.6218 (J kg^{-1} K^{-1})
Solid constant-pressure specific heat	385 (J kg^{-1} K^{-1}) [24]
Liquid thermal diffusivity	3.62E−05 (m^2 s^{-1})
Solid thermal diffusivity	7.63E−05 (m^2 s^{-1})
Laser absorptivity for flat surface	0.05

Table 2
Material properties of aluminum.

Property	Value
Melting temperature	933.47 (K)
Normal boiling temperature	2792 (K)
Critical point temperature	7963 (K)
Liquid density	2333 (kg m^{-3})
Solid density	2700 (kg m^{-3})
Kinematic viscosity	4.43635E−07 (m^2 s^{-1}) [25]
Surface tension	$0.860 - 0.000115 \times (T - 933.47)$ (N m^{-1}) [26]
Latent heat of vaporization	1.09E+07 (J kg^{-1})
Latent heat of fusion	3.97E+05 (J kg^{-1})
Solid thermal conductivity	237 (W m^{-1} K^{-1})
Liquid thermal conductivity	93.752 (W m^{-1} K^{-1})
Liquid constant-pressure specific heat	1255.2 (J kg^{-1} K^{-1})
Solid constant-pressure specific heat	896.9607116 (J kg^{-1} K^{-1})
Liquid thermal diffusivity	3.20E−05 (m^2 s^{-1})
Solid thermal diffusivity	9.79E−05 (m^2 s^{-1})
Laser absorptivity for flat surface	0.07

A CW single mode fiber laser with a focused beam diameter of 11 μm is used and it is moving in positive x direction. A Gaussian laser beam distribution is assumed and shown in Fig. 4. The grids for multiple reflection calculations are much finer than the main grid for the sake of a good resolution of solutions. The distance of grid for the laser beam is 0.1062 μm. Each mesh has different laser

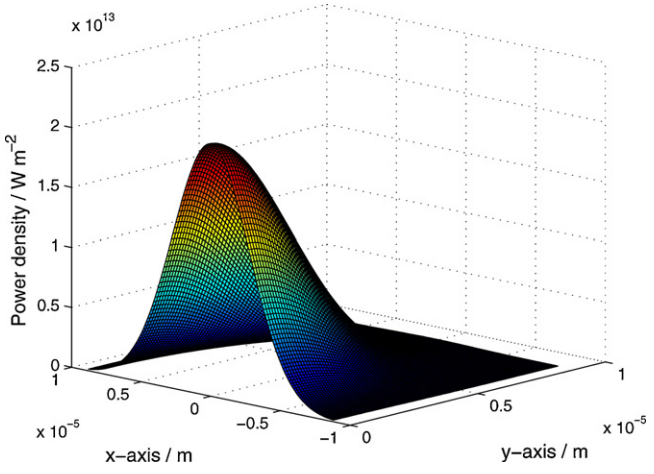

Fig. 4. Gaussian laser power density distribution.

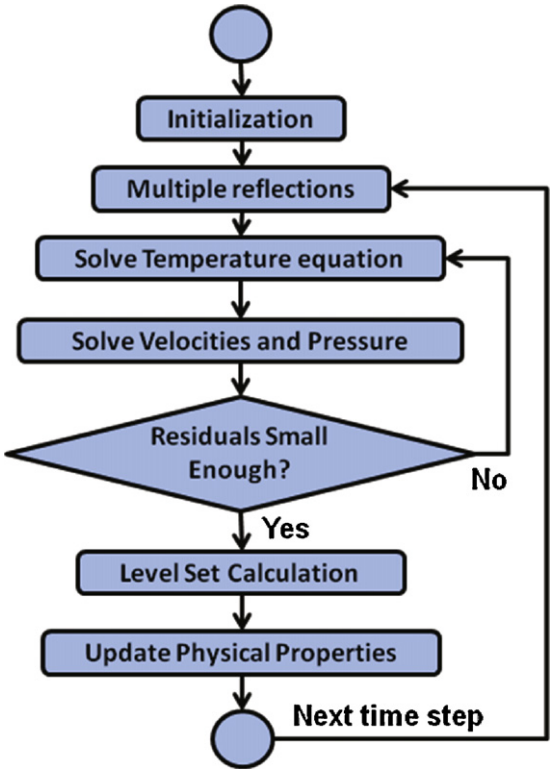

Fig. 5. Flow diagram of the solution procedure in each time step.

power density and the ray tracing technique is applied to the laser beam at each mesh to demonstrate the multiple reflections. The ranges of the laser power and scanning speed are 50–450 W and 1000 mm s^{-1} to 5000 mm s^{-1}, respectively. Discretization of the governing equations is accomplished using an implicit finite difference method. The conjugated Gradient Stabilized (CGSTAB) method and Semi-Implicit Method for Pressure-Linked Equation Consistent (SIMPLEC) are adopted to solve the matrix equation and coupled pressure-velocity fields on the staggered grid system, respectively. Furthermore, the spatial derivative of the level set equation is discretized with a second-order space convex scheme [20]. Finally, the value of c for all of the material properties is taken as 1 and $7 \times \min(\Delta z)$ is chosen for ε in this study to smooth the material properties. Δz is the smallest mesh size.

A flow diagram of the solution procedure in one time step is shown in Fig. 5 At the beginning of the simulation, initialization is completed to tabulate the variables on the Knudsen layer and to assign the simulation parameters. After the initialization, multiple reflections are executed. The temperature and velocities are solved sequentially in an inner loop with coupled solutions until their computational residuals satisfy certain criteria. Note that a maximum iteration is set to prevent unnecessary computations due to slow convergence, even though the residual values may not be satisfied. After obtaining temperature, velocity, and pressure, level set is calculated with the value of evaporation and convection that affects interface deformation. Finally, physical properties are updated with a given liquid mass fraction. This procedure is repeated until it satisfies the designated computation time.

The thicknesses of the copper and aluminum are assumed to be 10 μm and 15 μm, respectively. Variable laser parameters are power and scanning speed. The combinations of the simulation conditions are tabulated in Table 3 for copper and aluminum. When the depth of the deep penetration hole reaches the thicknesses of the substrate materials, called a full penetration cutting, penetration time is provided following simulation termination. When there is partial cutting, maximum penetration depth during the simulation is obtained first, and then the corresponding penetration time is obtained. Simulation results are summarized in Tables 4 and 5.

Table 3
Laser processing parameters for simulations on copper and aluminum.

Sim #	Copper		Aluminum	
	Power (W)	Speed (mm s^{-1})	Power (W)	Speed (mm s^{-1})
1	200	5000	100	5000
2	250	5000	150	5000
3	300	5000	200	5000
4	350	5000	250	5000
5	400	5000	300	5000
6	450	5000	350	5000
7	100	3000	50	3000
8	150	3000	100	3000
9	200	3000	150	3000
10	250	3000	200	3000
11	300	3000	250	3000
12	50	1000	50	1000
13	100	1000	100	1000
14	150	1000	150	1000
15	200	1000	200	1000
16	250	1000	250	1000

Table 4
Simulation results of laser cutting penetration time and depth for copper.

Sim #	Penetration	
	Time (μs)	Depth (μm)
1	1.8819	0.957
2	6.7452	4.787
3	0.9064	10.000
4	0.5452	10.000
5	0.4308	10.000
6	0.3762	10.000
7	0.0000	0.000
8	3.2125	0.531
9	6.7681	1.808
10	4.3982	10.000
11	0.8228	10.000
12	0.0000	0.000
13	0.0000	0.000
14	0.7176	0.106
15	6.8708	2.233
16	3.5166	10.000

Table 5
Simulation results of laser cutting penetration time and depth for aluminum.

Sim #	Penetration	
	Time (μs)	Depth (μm)
1	0.4576	1.382
2	0.3913	15.000
3	0.2541	15.000
4	0.2006	15.000
5	0.1728	15.000
6	0.1606	15.000
7	3.5509	1.382
8	0.4102	1.382
9	0.4018	15.000
10	0.2672	15.000
11	0.2101	15.000
12	3.1564	1.382
13	8.5736	1.808
14	0.3577	15.000
15	0.2498	15.000
16	0.2170	15.000

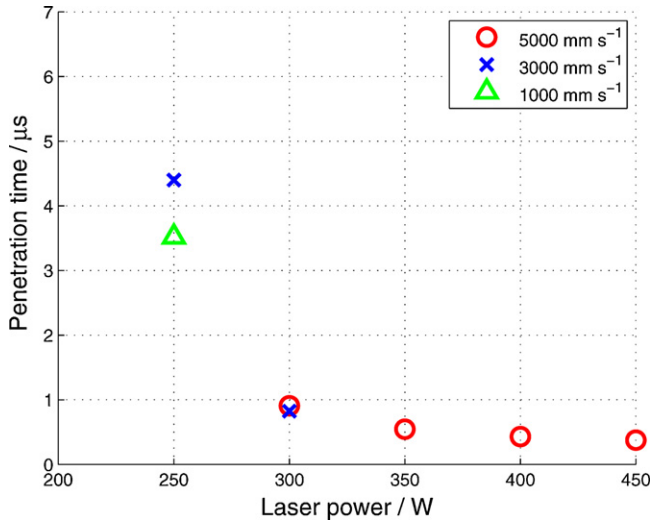

Fig. 6. Laser cutting penetration time for copper.

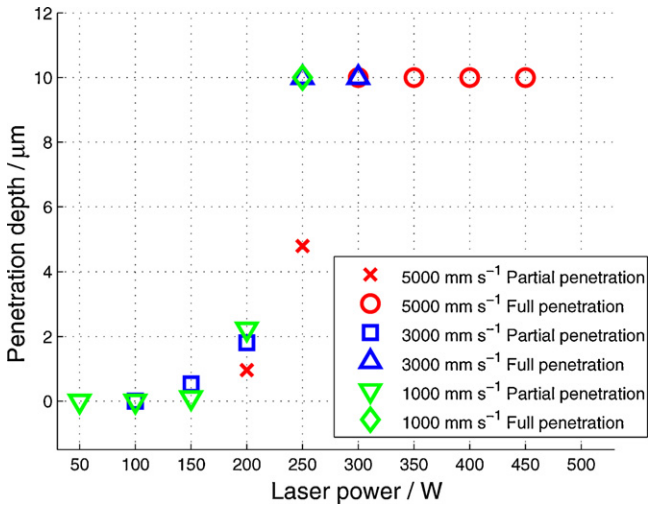

Fig. 8. Laser cutting penetration depth for copper.

4.2. Thresholds for cutting

The laser power and scanning speed thresholds for the full penetration cutting are obtained as shown in Tables 4 and 5. For copper, laser power between 250 W and 300 W is the threshold for 5000 mm s^{-1} scanning speed. Laser power between 200 W and 250 W is the threshold for both 3000 mm s^{-1} and 1000 mm s^{-1} scanning speeds. For aluminum, laser power between 100 W and 150 W is the threshold for 5000, 3000, and 1000 mm s^{-1}.

Laser–material interaction characteristics can be derived for both materials from these thresholds. Interaction time and laser intensity are closely related to laser speed and power. Since the thresholds for copper vary by scanning speed and laser power, interaction time and laser intensity are both effective factors. However, the laser power thresholds for aluminum are the same regardless of the given laser scanning speeds. This indicates that the aluminum laser cutting is more affected by laser intensity than the interaction time. Therefore, both interaction time and laser intensity are important for the copper laser cutting. Moreover, the aluminum laser cutting is highly influenced by the laser intensity.

4.3. Penetration time

Penetration times of full penetration cutting for copper and aluminum are presented in Figs. 6 and 7, respectively. The total penetration times during full penetration cutting for copper and aluminum have significant differences. The penetration times for aluminum are always less than 1 μs. On the other hand, only when laser power is greater than 300 W is penetration time less than 1 μs for copper.

For copper, the penetration time decreases exponentially when laser power is increased from 250 W to 450 W. For a laser power of 250 W, no full penetration cutting is obtained with a 5000 mm s^{-1} scanning speed. Moreover, the difference in penetration time between 3000 mm s^{-1} and 1000 mm s^{-1} scanning speeds is larger than other laser power cases. For a laser power of 300 W, slight differences in the penetration time are seen among the 5000, 3000, and 1000 mm s^{-1} scanning speeds.

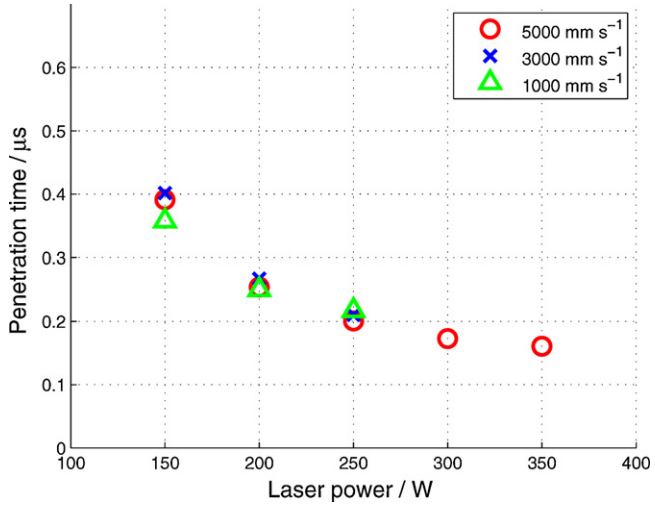

Fig. 7. Laser cutting penetration time for aluminum.

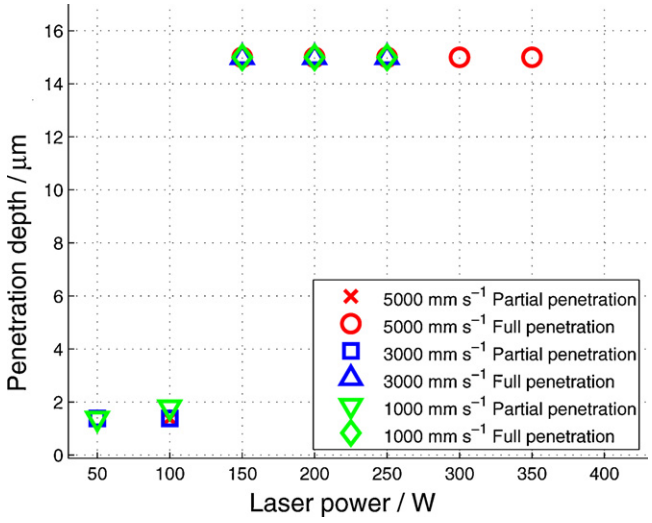

Fig. 9. Laser cutting penetration depth for aluminum.

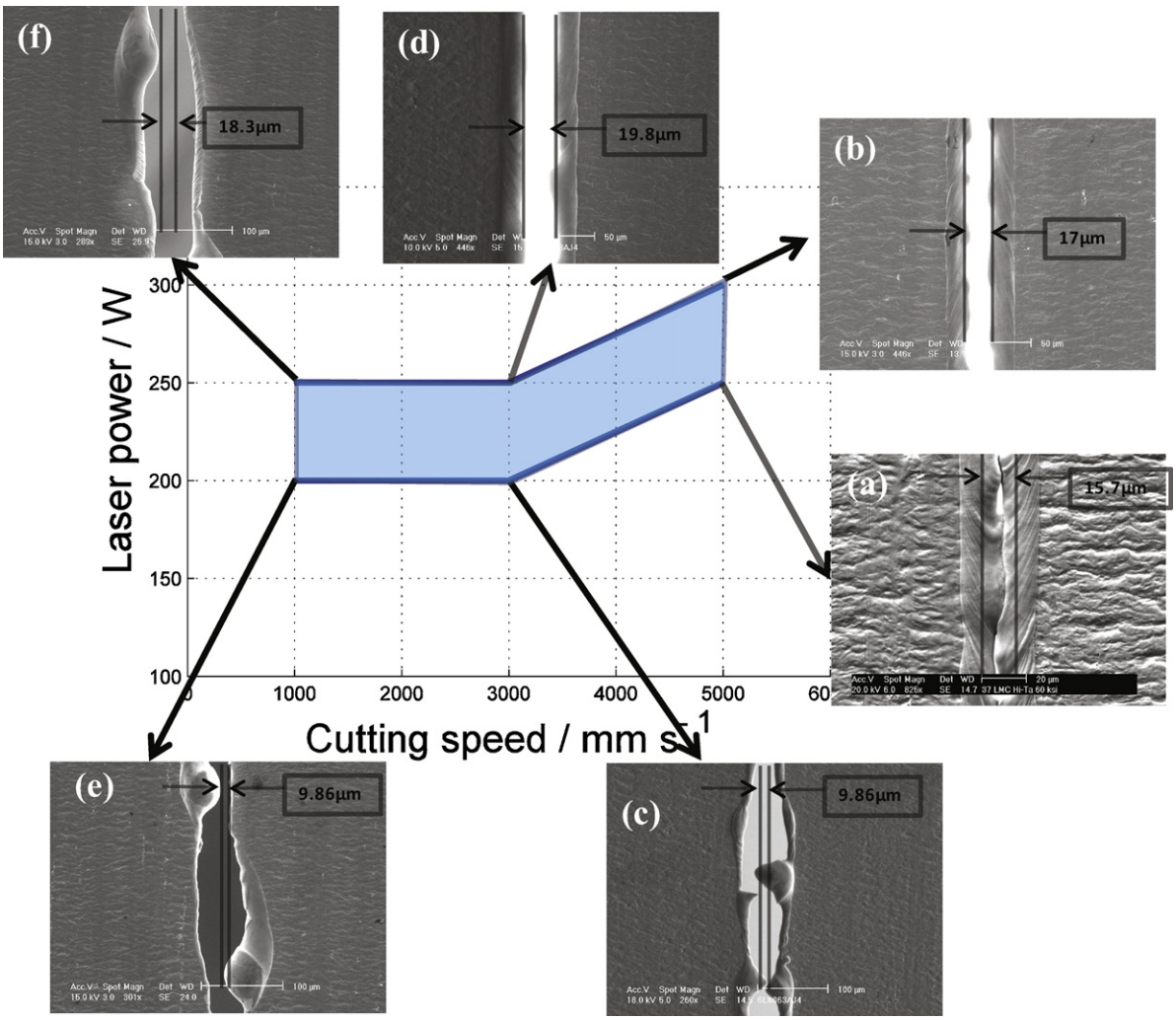

Fig. 10. Threshold and kerf width based on simulation results and experimental results of laser cutting on copper – dashed line is the kerf width of the simulation (a) 250 W, 5 m s^{-1}; (b) 300 W, 5 m s^{-1}; (c) 200 W, 3 m s^{-1}; (d) 250 W, 3 m s^{-1}; (e) 200 W, 1 m s^{-1}; (f) 250 W, 1 m s^{-1}.

For the aluminum case, the overall trend is the same as the copper case. However, the aluminum case shows a smoother decrease of penetration time with increasing laser power. While the copper case exhibits significant differences in penetration time with the laser powers of 250 W and 300 W, almost no differences in penetration time for the aluminum case are observed.

These results show again that the copper may have both interaction time and laser intensity dependent processes, and the aluminum may have only a laser intensity dependent process, likely due to absorption coefficients. The absorption coefficients for a wavelength of 1.070 μm of copper and aluminum are 0.05 and 0.07, respectively. The higher the absorption coefficient of the material, the more the energy that can be deposited on the material with the aid of multiple reflections. Therefore, aluminum is penetrated more rapidly than copper, even though aluminum foils are thicker.

4.4. Penetration depth

Full penetration cutting is obtained when the depth of the penetration hole reaches the materials' thicknesses, which are 10 μm and 15 μm for copper and aluminum, respectively. Once full penetration occurs, the penetration depths are automatically assigned. However, partial penetration, which is less penetration depth than the specimens' thicknesses, is obtained if insufficient energy is provided. Therefore, a relationship between the laser operating parameters and the penetration depths could be observed. These results for copper and aluminum are shown in Figs. 8 and 9, respectively. Furthermore, numerical values are shown in Tables 4 and 5.

For copper, the partial penetration depth increases exponentially when increasing the laser power. Values of the partial penetration vary from 0.106 μm to 4.797 μm, which is half of the specimen thickness. On the other hand, for aluminum, the partial penetration and full penetration cutting are clearly distinguished between 100 W and 150 W. The maximum partial penetration depth is 1.808 μm, which is 12% of the specimen thickness. From these results, we conclude again that the aluminum laser cutting is laser intensity dependent.

These results may be possible due to the materials' properties, such as absorptivity and melting points. Since aluminum has a high absorptivity as well as low melting and boiling points compared to copper, aluminum absorbs more energy. Once aluminum absorbs enough energy, the material is evaporated at a relatively fast speed. Therefore, the aluminum laser cutting shows clear differences between partial penetration and full penetration cutting.

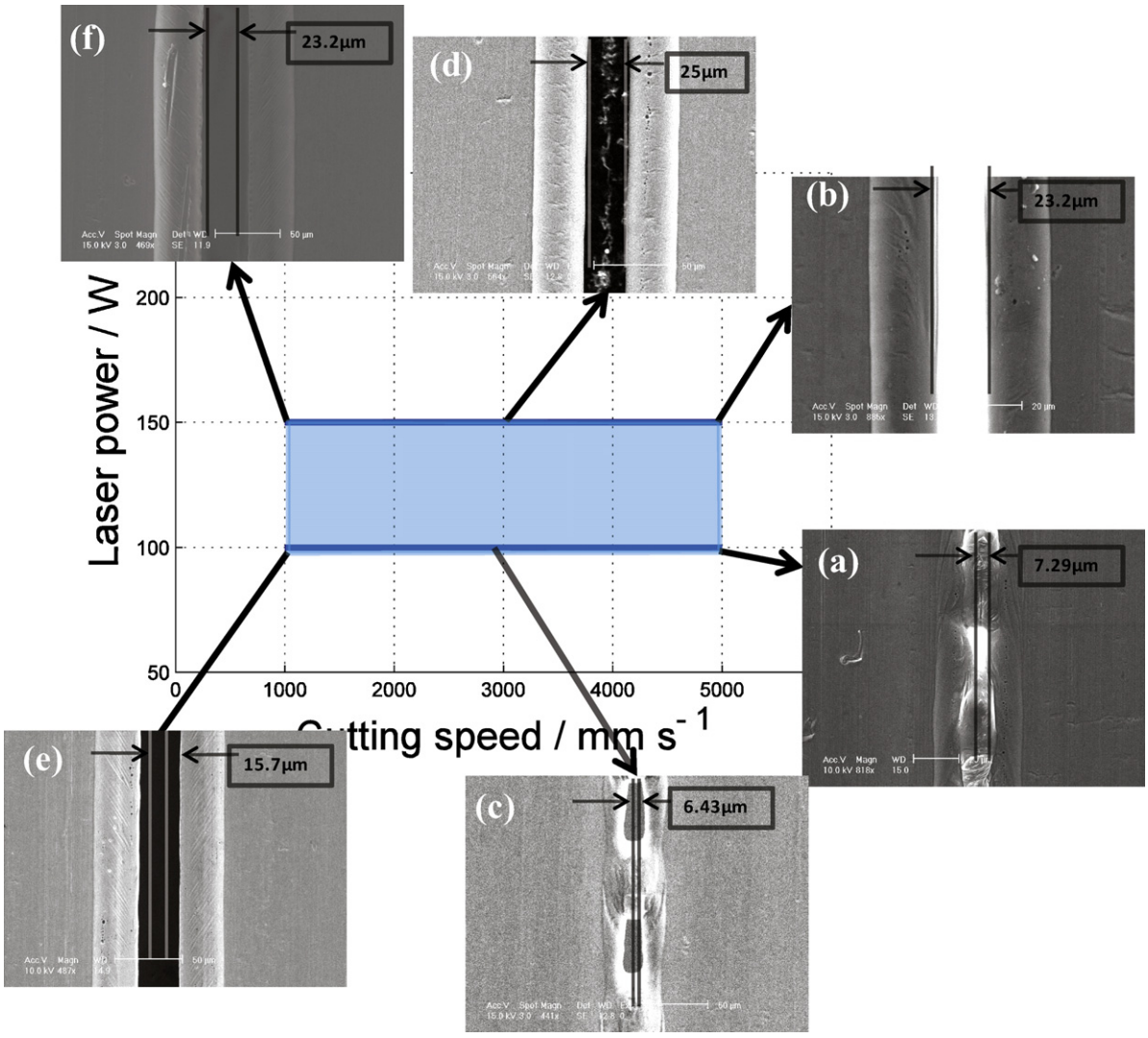

Fig. 11. Threshold and kerf width based on simulation results and experimental results of laser cutting on aluminum – dashed line is the kerf width of the simulation (a) 100 W, 5 m s^{-1}; (b) 150 W, 5 m s^{-1}; (c) 100 W, 3 m s^{-1}; (d) 150 W, 3 m s^{-1}; (e) 100 W, 1 m s^{-1}; (f) 150 W, 1 m s^{-1}.

4.5. Experimental validation

A series of linear laser cutting tests of the current collector materials and single side-coated electrodes are performed for validation with combinations of the laser parameters, as shown in Table 4. Here the laser power is the calibrated power output on the workpiece and includes all the beam delivery losses. During all cutting tests, the focus of laser beam was positioned on the surface of the electrode foil material. The length of cut was fixed at 25 mm and only a single pass of laser beam was used for cutting. The start and stop regions of the cut length were not considered for analysis to avoid any effects of scanner acceleration and deceleration at high speeds. To ensure accuracy of test results, cutting tests were repeated. Among these experimental results, SEM analysis is done for the cases that have laser power and laser scanning speeds near to full penetration cutting thresholds. The threshold, which is highlighted area, and top view of the copper laser cuttings are shown in Fig. 10, using a different combination of laser parameters. The kerf widths obtained from the aluminum laser cutting simulations. The kerf widths of the experimental and simulation results show a good agreement for the full penetration of high-speed cutting cases Fig. 10(a) shows almost no cutting. The small area of full penetration is barely seen. Reattachments in the cut surface are shown in Fig. 10(c). A bubble-shape recast is observed with inconsistent kerf width in Fig. 10(e). This bubble-shape recast creates the bad cut surface of the electrodes so that battery performances could be deteriorated. On the other hand, Fig. 10(b) and (d) shows clear cutting and consistent kerf width. Even though 250 W and 1000 mm s^{-1} laser beam create the full penetration, bubble-shape recast is seen in Fig. 10(f).

Fig. 11 shows the threshold, which is highlighted area, and top view of the laser cutting of aluminum. Dashed lines depict the kerf widths obtained from the simulation. The kerf widths of the experimental and simulation results show a good agreement for the full penetration cases. Fig. 11(a) shows reattachment at the cutting zone. These reattachments bridge the two separated foils. Depending on the size of this reattachment, some of them dissociate easily when merely touched. Similar phenomena could be observed in Fig. 11(c). Thus, we could treat these cases as the partial penetration cutting. On the other hand, full penetration cutting is achieved in Fig. 11(b), (d), and (f), which are 150 W laser power cases, as predicted by the simulation results. However, Fig. 11(e) shows full penetration cutting.

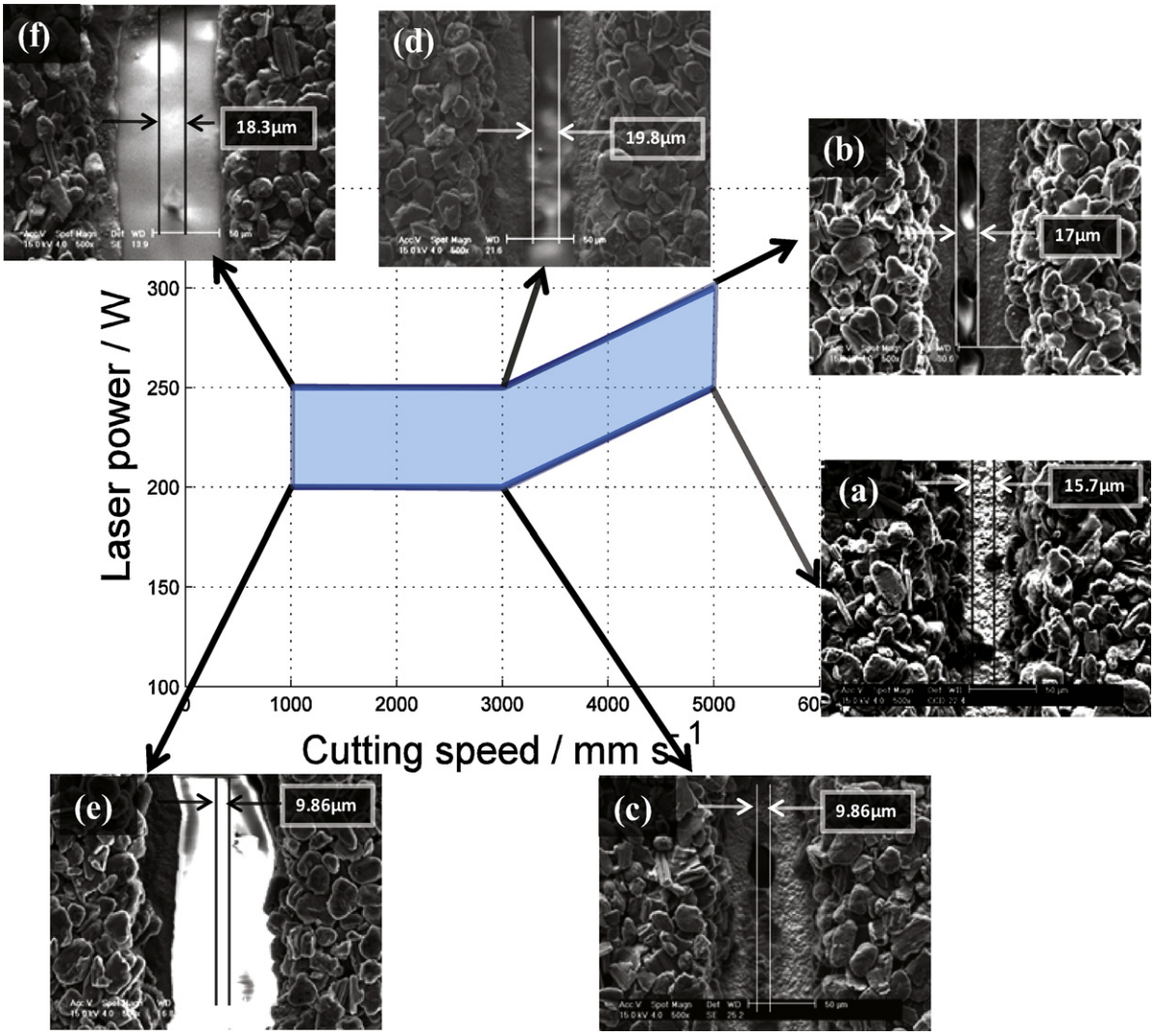

Fig. 12. Threshold and kerf width based on simulation results and experimental results of laser cutting on anode – dashed line is the kerf width of the simulation (a) 100 W, 5 m s^{-1}; (b) 150 W, 5 m s^{-1}; (c) 100 W, 3 m s^{-1}; (d) 150 W, 3 m s^{-1}; (e) 100 W, 1 m s^{-1}; (f) 150 W, 1 m s^{-1}.

Therefore, simulation results match well with experimental studies for the high speed laser cutting, such as 5000 mm s^{-1} and 3000 mm s^{-1}, of the current collector materials. However, there is a discrepancy for the low speed cutting, such as 1000 mm s^{-1}. The reason for this might be that the mathematical model used a constant absorption coefficient. Therefore, including a temperature dependent absorption coefficient might improve the mathematical model for low speed cutting.

The kerf widths and thresholds of current collector materials obtained by simulation are compared to the experimentally obtained results of current collector materials in the presence of the active electrode materials to validate the proposed mathematical model in a more realistic situation. The threshold of copper laser cutting and top view of the single side-coated anode laser cuttings are shown in Fig. 12. Only graphite is sublimated in Fig. 12(a). Fig. 12(b) shows the partial cutting of copper. Thus, the laser power of 300 W provides not enough energy to obtain full penetration cutting with the 5000 mm s^{-1} scanning speed. With the 3000 mm s^{-1} scanning speed, simulation results match well with experimental studies as shown in Fig. 12(c) and (d). Although the kerf width of copper in Fig. 12(d) shows a good agreement, wider kerf widths are observed for graphite. Both Fig. 12(e) and (f) show full penetration cutting with 3.7 times wider kerf widths compared to simulation results.

Fig. 13 shows the thresholds of aluminum laser cutting and top view of the single side-coated cathode laser cuttings. No cutting is observed in Fig. 13(a). Regardless of laser scanning speeds, the laser power of 150 W provides full penetration cutting as seen in Fig. 13(b), (d), and (f). This full penetration is predicted by the simulation results. Furthermore, the kerf widths of aluminum obtained experimentally and numerically are in good agreement, as shown in Fig. 13(b), (d), and (f). However, Fig. 13(c) and (e) shows full penetration cutting and these are different to results estimated by simulation.

Simulation and experimental results of copper with the single side-coated graphite are in good agreement in the case of the 3000 mm s^{-1} scanning speed. In addition, simulation results of aluminum with single side-coated $LiCoO_2$ match well with experimental studies in the case of 5000 mm s^{-1}. The other cases show discrepancies. These discrepancies can be caused by the different absorption coefficients between current collector and active electrode materials. Furthermore, the sublimation characteristic of graphite might affect these discrepancies. Finally, the composition variation of current collector materials between the interface

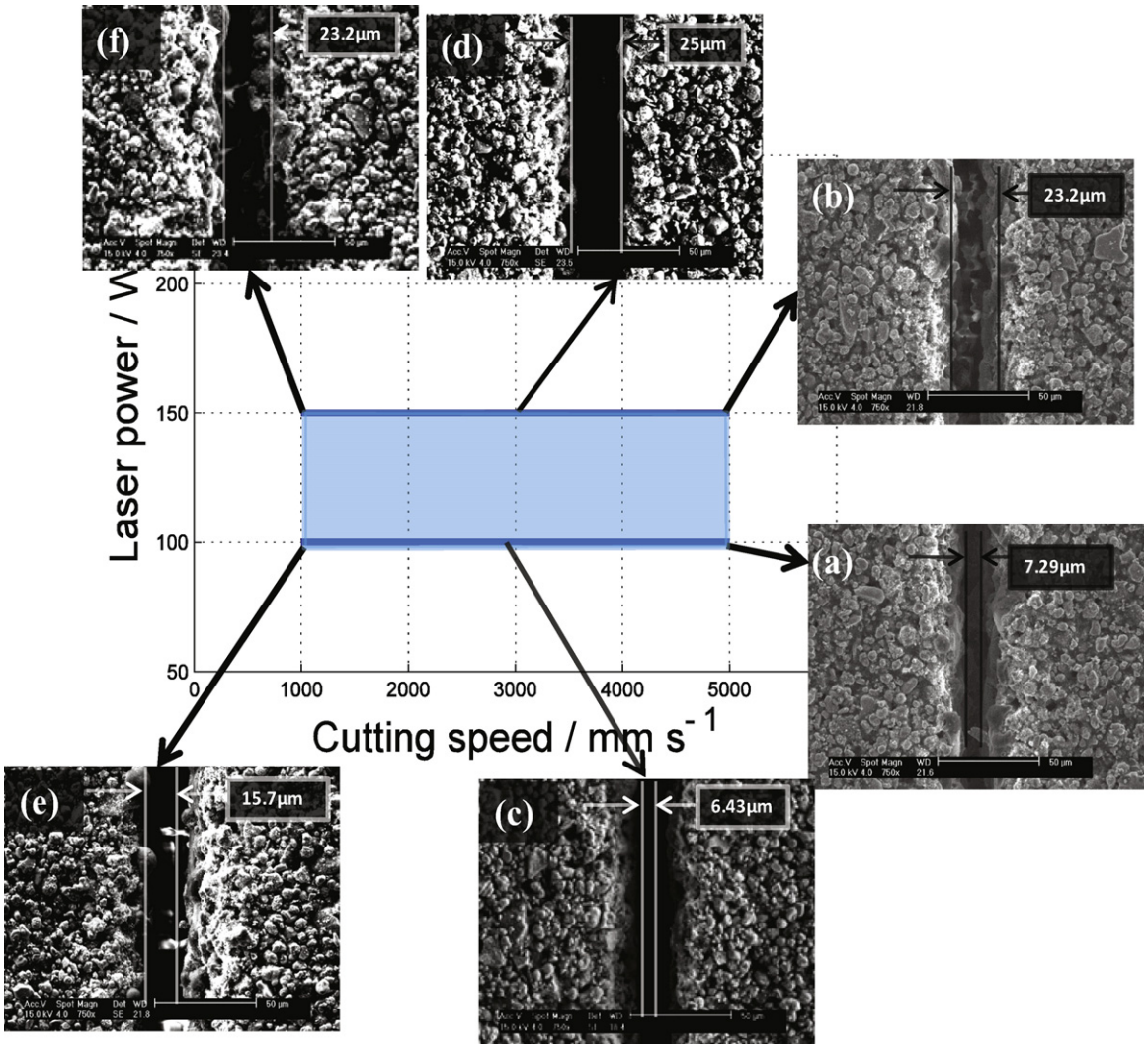

Fig. 13. Threshold and kerf width based on simulation results and experimental results of laser cutting on cathode – dashed line is the kerf width of the simulation (a) 100 W, 5 m s^{-1}; (b) 150 W, 5 m s^{-1}; (c) 100 W, 3 m s^{-1}; (d) 150 W, 3 m s^{-1}; (e) 100 W, 1 m s^{-1}; (f) 150 W, 1 m s^{-1}.

of current collector and active electrode materials may result in discrepancies between simulation and experimental results.

5. Conclusions

The numerical studies of the mathematical model have been described for cutting of copper and aluminum foils with a single mode laser, which are used as current collectors of the lithium-ion battery electrodes. The mathematical model includes fluid flow, heat transfer, evaporation, multiple internal reflections, free surface evolution, and surface forces with proper material phase changes. Using this proposed mathematical model, the threshold laser parameters for cutting as well as penetration time and depth have been investigated. Given the presented results, we could conclude that the copper laser cutting is a laser intensity and interaction time dependent process. The aluminum laser cutting depends more on laser intensity than interaction time. The proposed mathematical model is validated experimentally. Experimental and simulation results of pure current collector materials show a strong agreement for the high-speed cutting cases. A small discrepancy observed for low-speed cutting can be improved by modifying the constant absorption coefficient to be a temperature dependent absorption coefficient. A bubble-shape recast observed from experimental results could deteriorate the cut surface of electrodes for lithium-ion batteries. Simulation results of pure copper are in good agreement with experimental results of pure copper with single side-coated graphite when a laser scanning speed is 3000 mm s^{-1}. Experimental results of pure aluminum with single side-coated $LiCoO_2$ match well with simulation results of pure aluminum when a laser scanning speed is 5000 mm s^{-1}. Taking into consideration active electrode materials in the proposed mathematical model can improve the simulation results for current collector materials.

This study could be utilized as a guideline to obtain good quality of a cut surface so that clear cut edge without reattachments and bubble-shape recasts can prevent the catastrophic failure of the entire module. Therefore, the desired quality of a cut surface can be obtained without defects by controlling the laser power and scanning speed. Furthermore, an understanding of the influences of the laser parameters on the laser cutting for the current collector materials would be used for further investigation of the electrode cutting behaviors.

Acknowledgments

This effort was supported by the University of Michigan – Fraunhofer Alternative Energy Technologies for Transportation Program

(AETT Program). The authors appreciate the support from our sponsors.

References

[1] R. Patwa, H.J. Herfurth, H. Pantsar, S. Heinemann, J. Mazumder, D. Lee, Proceedings of the ICALEO, Anaheim, CA, 2010.
[2] M. Alamgir, A.M. Sastry, SAE Convergence, Detroit, MI, 2008.
[3] M. Winter, R.J. Brodd, Chemical Reviews 104 (2004) 4245–4269.
[4] H.J. Herfurth, R. Patwa, H. Pantsar, Proceedings of the LPM, Germany, 2010.
[5] H.J. Herfurth, R. Patwa, H. Pantsar, S. Heinemann, G. Newaz, Proceedings of the ICALEO, Temecula, CA, USA, 2008.
[6] M. Luetke, V. Franke, A. Techel, T. Himmer, U. Klotzbach, A. Wetzig, E. Beyer, Physics Procedia 12 (2011) 286–291.
[7] H. Ki, P.S. Mohanty, J. Mazumder, Journal of Physics D: Applied Physics 34 (2001) 364–372.
[8] H. Ki, P.S. Mohanty, J. Mazumder, 20th Icaleo 2001, Congress Proceedings, vols. 92 and 93, 2001, pp. 933–942.
[9] H. Ki, P.S. Mohanty, J. Mazumder, Metallurgical and Materials Transactions A: Physical Metallurgy and Materials Science 33 (2002) 1817–1830.
[10] H. Ki, P.S. Mohanty, J. Mazumder, Metallurgical and Materials Transactions A: Physical Metallurgy and Materials Science 33 (2002) 1831–1842.
[11] H. Ki, P.S. Mohanty, J. Mazumder, Journal of Laser Applications 14 (2002) 39–45.
[12] H. Ki, P.S. Mohanty, J. Mazumder, Numerical Heat Transfer Part B: Fundamentals 48 (2005) 125–145.
[13] W.D. Bennon, F.P. Incropera, International Journal of Heat and Mass Transfer 30 (1987) 2161–2170.
[14] S. Osher, J.A. Sethian, Journal of Computational Physics 79 (1988) 12–49.
[15] J.A. Sethian, Level Set Methods and Fast Marching Methods, 2nd ed., Cambridge University Press, Cambridge, 1999.
[16] C.J. Knight, AIAA Journal 17 (1979) 519–523.
[17] T. Ytrehus, S. Ostmo, International Journal of Multiphase Flow 22 (1996) 133–155.
[18] R. Fabbro, K. Chouf, Journal of Applied Physics 87 (2000) 4075–4083.
[19] S.V. Patankar, Numerical Heat Transfer and Fluid Flow, Hemisphere Pub. Corp., McGraw-Hill, Washington, New York, 1980.
[20] J.A. Sethian, Level Set Methods and Fast Marching Methods: Evolving Interfaces in Computational Geometry, Fluid Mechanics, Computer Vision, and Materials Science, 2nd ed., Cambridge University Press, Cambridge, U.K., New York, 1999.
[21] M.J. Assael, K. Kakosimos, R.M. Banish, J. Brillo, I. Egry, R. Brooks, P.N. Quested, K.C. Mills, A. Nagashima, Y. Sato, W.A. Wakeham, Journal of Physical and Chemical Reference Data 35 (2006) 285–300.
[22] B.B. Alchagirov, A.M. Chochaeva, V.B. Bekulov, K.B. Khokonov, High Temperature 41 (2003) 472–476.
[23] R. Brandt, G. Neuer, International Journal of Thermophysics 28 (2007) 1429–1446.
[24] E.H. Buyco, F.E. Davis, Journal of Chemical and Engineering Data 15 (1970) 518.
[25] N.Y. Konstantinova, P.S. Popel, D.A. Yagodin, High Temperature 47 (2009) 336–341.
[26] T. Matsumoto, H. Fujii, T. Ueda, M. Kamai, K. Nogi, Measurement Science & Technology 16 (2005) 432–437.